# Theoretical Study on Enhancement of Sensing Capability of Plasmonic Dimer Au Nanoparticles with Amphiphilic Polymer Brushes

Eun Min Go,[†,⊥] Tae Kyung Lee,[†,⊥] Sa Hoon Min,[†,⊥] Woo Cheol Jeon,[†] Byeong-Su Kim,*[,†,‡] Min Sun Yeom,*[,§] and Sang Kyu Kwak*[,†,∥]

[†]School of Energy and Chemical Engineering, and [‡]Department of Chemistry, School of Natural Science, Ulsan National Institute of Science and Technology (UNIST), 50 UNIST-gil, Ulsan 44919, Republic of Korea

[§]Department of Supercomputing Application, Supercomputing Service Center, Division of National Supercomputing R&D, Korea Institute of Science and Technology Information (KISTI), 245 Daehak-ro, Daejeon 34141, Republic of Korea

[∥]Center for Multidimensional Carbon Materials, Institute for Basic Science (IBS), Ulsan 44919, Republic of Korea

Ⓢ *Supporting Information*

**ABSTRACT:** Au nanoparticle (Au-NP) sensors need a high surface plasmon resonance intensity and a low steric effect for efficient labeling in sensors. Since dimers meet these requirements, we have theoretically studied the self-assembly of monomer and dimer Au-NPs by considering influential factors such as Au-NP size, polymer thickness, and gap distance between dimer Au-NPs. In order to control the monomerization and dimerization of spherical Au-NPs and their sizes via self-assembly, two polymers (hydrophilic PEG and hydrophobic PMMA) were grafted on the Au-NPs as amphiphilic brushes. Computational methods of dissipative particle dynamics and discrete dipole approximation were employed for virtual self-assembly and theoretical analyses of plasmons related to sensing properties, respectively. We found that the bigger Au-NPs were obtained when the amounts of each polymer were roughly identical and the gap distance between Au-NPs in the dimer was shorter when the amount of PMMA was reduced within the condition of dimerization. This theoretical study revealed an optimal near-contact distance for Au-NPs@PMMA/PEG, where the electron tunneling effect was minimized, and reported unseen roles of polymers and plasmons, which consequently allowed achieving a highly efficient Au-NP dimer sensor.
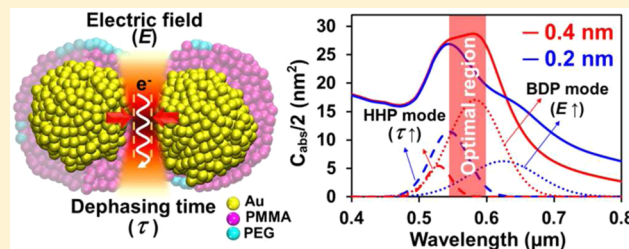
## ■ INTRODUCTION

Au nanoparticles (Au-NPs) have been widely used in fields related to electronics and photonics. Among several important factors under consideration, the size and shape controls have been the important issues, particularly in nanofabrication processes.[1,2] When Au-NPs are larger than ~2 nm,[1] the surface plasmon resonance (SPR) appears and the SPR absorbance becomes detectable. Also, the SPR absorbance of Au-NPs can be tunable by changing the size or shape. Therefore, Au-NPs have been applied in sensors,[3] colorimetric detection,[4] and labeling in biosystems.[5−7] For the application of NP, large size NPs (10−100 nm) are commonly used due to their high SPR intensity, since the absorbance intensity and red-shift of the peak wavelength increase with increasing particle size.[8] In contrast, the labeling efficiency increases with a decrease in size because of less steric effect.[9] When the NPs are smaller than 10 nm, quantum size effects (i.e., intrinsic size, spatial nonlocality, etc.) become important on Au-NPs due to the comparable length regarding the mean free path of conduction electrons.[10] These effects influence on the sensing capabilities of Au-NPs by changing the width of spectral peaks, resonance peak wavelength, and electric field intensity. Especially, intrinsic

size effect makes the spectral peaks broaden and reduces the peak intensity. Nonlocal effect influences the peak wavelength by inducing the blue-shift and reduces the electric field intensity over the Au-NP surface. Thus, the quest to achieve a high SPR intensity with a minimal steric effect remains a challenge in the course of making good SPR-based sensors. A synthesis method exists to help overcome the above-mentioned limitations. An Ag staining strategy,[10−12] where Ag is coupled with Au-NPs to enhance the SPR intensity, could be used. However, complex experimental steps are generally involved when compared to nonstaining methods, which do not involve the process of coating of silver or other plasmonic materials on the surface of Au-NP.

In that regard, the dimerization of Au-NPs is a promising approach to obtain high SPR intensities with reduced steric effects. The SPR absorbance peak is increased due to the plasmonic coupling in dimers when two NPs are in close proximity, and thus sensing becomes more accurate than the
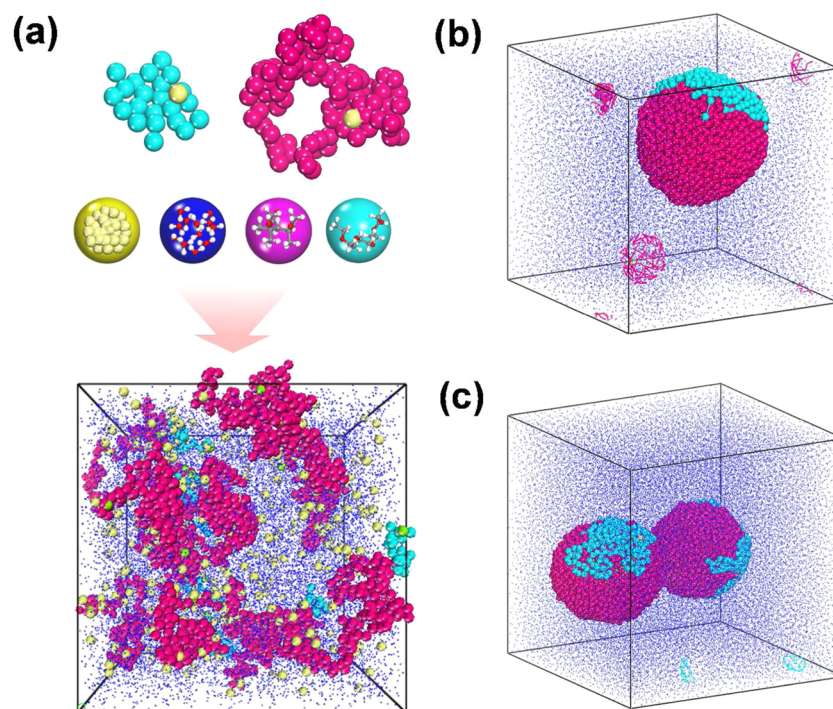
**Figure 1.** (a) Bead models of DPD and an initial state of the simulation. The Au bead (yellow) conceptually contains 28 Au atoms, and the water bead (blue) conceptually contains 12 water molecules. PEG and PMMA are composed of 22 and 110 beads, respectively, where a PEG bead (cyan) conceptually contains 5.2 constitutional units and a PMMA bead conceptually contains 2 constitutional units. (b) Self-assembled Au-NP@PMMA/PEG monomer from the DPD simulation with a total of 25 725 beads at 16.4, 75.6, and 8 vol % of Au, PMMA, and PEG, respectively, with excess water in a box of $20 \times 20 \times 20$ $R_c^3$, where $R_c$ is the cutoff radius (i.e., 1.026 nm). Polymer chains are 17 and 9 ea for PMMA and PEG, respectively. (c) Self-assembled Au-NP@PMMA/PEG dimer from the DPD simulation with a total of 51 110 beads with 27.4, 64.3, and 8.3 vol % of Au, PMMA, and PEG, respectively, with excess water in a box of $26 \times 26 \times 26$ $R_c^3$. Polymer chains are 26 and 18 ea for PMMA and PEG, respectively.

monomer case.[13] One of the methods for dimerization involves attaching polymer brushes, where polymer chains are grafted on the NP surface. This favors particle aggregation to form different morphologies.[14,15] The synthesis method consists of sequential steps of making Au-NP followed by grafting of the polymers. Conveniently, a single-step method is also available by mixing directly the aqueous polymer solution and Au precursors.[16,17] The latter method is particularly interesting since both size-control and Au-NP aggregation are simultaneously achieved. Accordingly, this single-step method was adopted in our study, in order to minimize the drawbacks of small-sized NP (i.e., low SPR intensity) by increasing the SPR intensity from self-assembled dimerization. In order to aggregate Au-NPs to a certain degree, we set an amphiphilic nature on the Au-NP using hydrophobic and hydrophilic polymers. The combination of hydrophobic PMMA and hydrophilic PEG has been shown to create amphiphilic Au-NPs, which are stable[18,19] and form dimers.[20,21] In practice, it is difficult to know the exact amount of polymers, resulting in a targeted degree of size-controlled NP aggregation through self-assembly. Furthermore, the synthesis task becomes more difficult if the gap distance between the two Au-NPs in the dimer is controlled to produce an efficient SPR absorbance since one needs to avoid the electron tunneling effect, which occurs in very short distances (i.e., below 0.4 nm).[22,23]

We used a theoretical approach in order to determine key information on the efficient SPR NP sensor by using two computational methods, namely dissipative particle dynamics (DPD) and discrete dipole approximation (DDA). Since self-assembly was a crucial phenomenon to synthesize the Au-NPs,

a coarse-grained (CG) simulation method was adopted. This allowed us to observe changes in the microphase including self-assembly, which is usually very time-consuming. We expected to obtain Au-NP between 2 and 10 nm, which could represent an average size. DPD is one of the most well-known CG methods, where a *bead* (i.e., super atom) is the building block for modeling materials. With appropriate repulsive forces exerted on modeled beads, it has been successfully applied to study liquidlike phases, polymers,[24−26] and colloidal Au-NPs.[27,28] The description of the DPD simulation is introduced in the Computational Methods section. DDA is a theoretical method to estimate optical properties of plasmonic materials responding to external electrical field through dipole moments of discretized dipoles.[29] The sensing capabilities were studied using absorption cross section ($C_{abs}$), detection accuracy, and electric field intensity ($|E(\omega)|^2/E_0^2$, where $E_0$ is the incident electric field and $E(\omega)$ is the induced electric field at a frequency ($\omega$)) in terms of grafted polymer thickness and composition. In the DDA calculation, we included three quantum effects (intrinsic size, spatial nonlocality, and electron tunneling) into the classical electrodynamics calculation in order to determine their influence on the sensing capability. The description of the DDA method and the detailed derivation for each quantum effect are introduced in the Computational Methods section.

## ■ RESULTS AND DISCUSSION

**Self-Assembly Studies of Monomer and Dimer Au-NP@PMMA/PEG via DPD.** With the bead model (Figure 1a), the monomer (Figure 1b) and dimer (Figure 1c) of Au-NP@

PMMA/PEG were self-assembled via the DPD simulation at room temperature. The time-based self-assembly processes are presented (Figures S2 and S3 and following note). (Note: We determined the formation time of the fully grown monomer, which took ~770 ns as shown from Figure S4a, by tracing the self-assembled number of Au beads with respect to the simulation time. The growth rate of the monomer was estimated, which is shown in Figure S4b. For this calculation, the Lifshitz−Slyozov−Wagner (LSW) model for Ostwald ripening was employed,[65] and the rate constant of growth of Au-NP was 0.75 nm/ns$^{1/3}$.) To check the reliability of the polymer models, we compared the radius of gyration ($R_g$) from PEG and PMMA with the experimental results.[30,31] Average $R_g$'s were in agreement with the literature values to within 5.9 and 16.2 error % for PEG and PMMA, respectively (Figure S5). Note that the large difference of $R_g$'s for PMMA was due to the bulk[32] and the grafted systems. Grafted Au beads were well located within 1 nm from the surface of the Au-NPs (Figure S6). The size of Au-NPs in the monomer (Figure 1b) was 5.5 nm as expected. Interestingly, PEG and PMMA segregated into each other, and PMMA was closer to the Au-NP surface due to its strong affinity to Au, as expected from smaller repulsion parameters (Table S1). The two Au-NPs in the dimer (Figure 1c) were formed with diameters of 5.6 and 5.9 nm, respectively, where PMMA acted as a linker between the two monomers.

Since the DPD simulation produced rather realistic results, we have thoroughly investigated the factors that influence the sensing capability. First, in order to increase the Au-NP size in the monomer system, the relative amount of the two polymers was varied, while fixing the amount of Au at 16.4 vol %. Figure 2 shows the influence of the PMMA quantity (vol %) on the
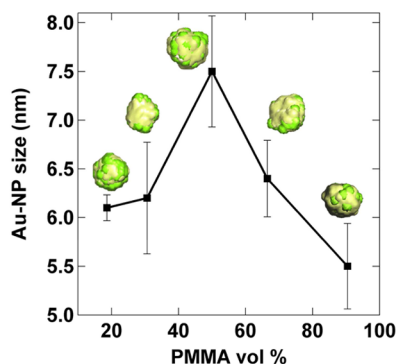


**Figure 2.** Plot of the size of Au-NP as a function of the relative vol % of PMMA to PEG at fixed 16.4 vol % of Au. Inset particles are snapshots of self-assembled Au-NPs. Green and light yellow colors represent grafted Au beads and original Au beads, respectively.

size of the Au-NPs. We found that the biggest Au-NPs were obtained using a nearly equivolumetric mixture of the two polymers. In these conditions, the chain length of the PMMA was about 5 times longer than that of the PEG. Hence, the number of PEG polymers was roughly 5 times larger than that of PMMA. Cheng et al.[20] explained that the growth of small-sized Au-NPs was due to a shielding effect of PEG, but from our results, the hydrophobic effect from PMMA could be equally treated. By varying the relative amounts of Au and two polymers, the formation composition for the Au-NP@PMMA/PEG dimer was obtained (Figure S7). The ternary phase diagram clearly shows that the relative amount of PMMA required for the formation of the dimer. The PMMA ranged

from 54.3 to 64.3 vol %, which was equivalent to a number of PMMA polymers between 20 and 28 ea (Table S2).

The gap distance between two Au-NPs in dimers can also affect the absorbance, so we conducted the following dimerization study. First, we found the distance criterion for the aggregation of dimer from two monomers. Two Au-NP@PMMA/PEG monomers with the size of Au-NP (i.e., 5.9 nm, the same system as in Figure 1c) were separately self-assembled at the gap distances of 12.4, 11.4, and 7.6 nm in water (Figure S8). The dimerization occurred when the gap distance was smaller than about 1.9 times the size of the monomer. By setting up the gap distance at 9.6 nm (i.e., smaller than 11.4 nm), two monomers with varying numbers of PMMA polymers (from 20 to 28 ea), which corresponded to the dimerization condition (Figure S7), were separately self-assembled. Figure 3
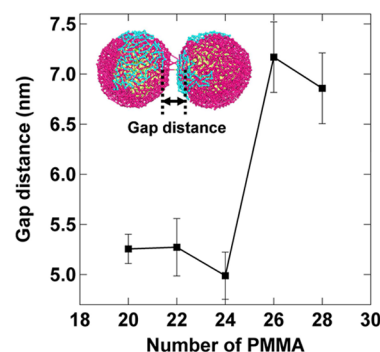


**Figure 3.** Gap distance vs the number of PMMA polymers at fixed 27.4 and 8.3 vol % of Au and PEG, respectively ((f) in Figure S7). The number of beads of Au and PEG were 1268 and 414, respectively. Yellow, cyan, and pink colors represent Au, PEG, and PMMA, respectively.

showed the gap distances between Au-NPs in dimers with respect to the number of PMMA polymers. We found that the distance between Au-NPs became closer when the number of PMMA was less than 25 ea, which demonstrated that the amount of PMMA may significantly affect the sensing capability of the dimer. Ghosh and Pal reported that the coupling plasmonic effect appeared when $d/R$ was smaller than 5, where $d$ is the center-to-center distance and $R$ is the NP radius.[33] Our dimer system, where $d/R$ was about 4.6, matched very well with their result.

**Prediction of Sensing Capabilities of Monomer and Dimer Au-NP@PMMA/PEG via DDA.** To elucidate the sensing capability, the sensing characteristics of absorbance, full width at half-maximum (fwhm), and electric field intensity were investigated for both monomer (Figure 4) and dimer (Figure 5) using DDA. Note that fwhm is the inverse of the detection accuracy[34] and the electric field intensity represents the sensitivity, which is the sensing strength at contact with objects. For the DDA calculation, we used the diameter of Au-NP as 7.6 nm, which was the largest size in monomer obtained from previous DPD simulation, for both monomer and dimer models. For monomer Au-NP, quantum effects (i.e., intrinsic size effect and nonlocal effect) were included due to the small size of Au-NP. Consequently, those effects lead to the decreases in $C_{abs}$ (Figure S9a) and $|E(\omega)|_{max}^2/E_0^2$ (Figure S9b) at the blue-shifted (~3.3 nm) peak wavelength. Furthermore, the detection accuracy was reduced due to the reduction of the total dephasing time of plasmon resonance,[35] as indicated by
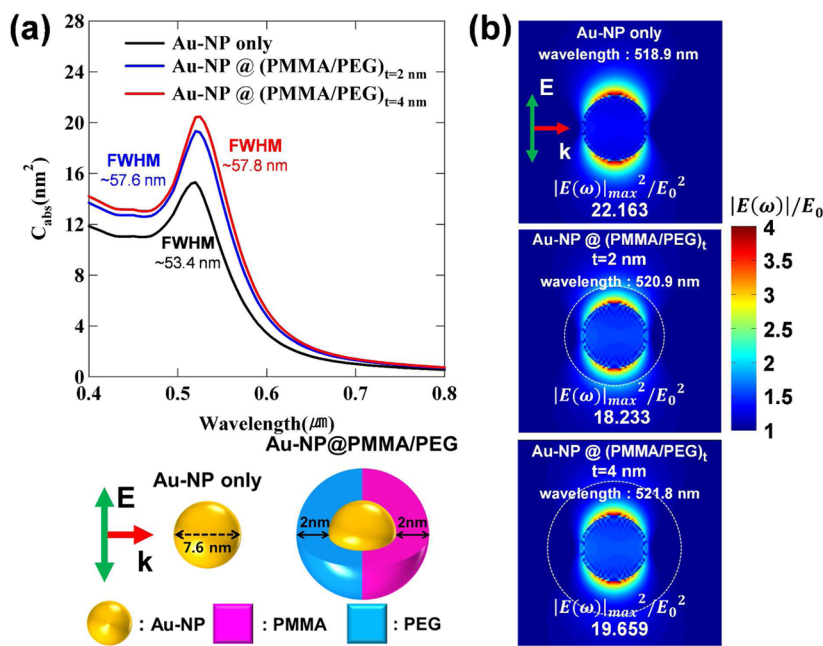
**Figure 4.** (a) Absorption cross sections ($C_{abs}$) of Au-NP (28 768 dipoles), Au-NP@(PMMA/PEG)$_{t=2\ nm}$ (102 208 dipoles), and Au-NP@ (PMMA/PEG)$_{t=4\ nm}$ (248 872 dipoles), where the subscript $t$ stands for the thickness of the polymer shell. The size of Au-NP and the thickness of the polymer shell are extracted from the maximum size (diameter = 7.6 nm) of self-assembled Au-NP in the DPD simulation from Figure 2. (b) Electric field contour plots at peak wavelengths from (a). White dashed lines represent the polymer shells. Directions of the electric field $E$ and the incident light $k$ are indicated with arrows. $E(\omega)$ is the induced electric field and $E_0$ is the external electric field as a reference. The subscript max represents the maximum value of $|E(\omega)|^2/E_0^2$.

the increased fwhm. Therefore, quantum effects resulted in lowering the sensitivity as well as the detection accuracy.

When the polymers were grafted as 2 nm thick shell on Au-NP, which was chosen from the result of our DPD simulation (∼1.8 nm), $C_{abs}$ was increased at the peak wavelength red-shifted by ∼2 nm and fwhm was increased (Figure 4a). When the thickness of the polymer shell was increased to 4 nm, $C_{abs}$ was increased further and the peak was red-shifted further by ∼2.9 nm with even broader fwhm. It clearly showed that the polymer shell intensified the absorbance spectra at the red-shifted wavelength but decreased the detection accuracy. Interestingly, for a thickness of 4 nm, the value of $|E(\omega)|_{max}^2/E_0^2$ near the Au-NP surface was increased in comparison with that for the 2 nm thickness (Figure 4b). We found that, when the polymer shell was thicker, the value of $|E(\omega)|_{avg}^2/E_0^2$ near the surface became higher since the thick shell helped to enhance the induced electric field inside the Au-NP by accommodating collective oscillation of plasmons (Figure S10). However, the enhanced electric field decayed non-monotonically through the polymer shell and finally became lower than that of Au-NP@(PMMA/PEG)$_{t=2\ nm}$ at ambient medium. Consequently, the sensitivity became the least for the thick polymer shell. Interestingly, we found ignorable effects of various core−shell models on absorbance spectra (i.e., at peak wavelengths, maximum difference of ∼1.04% for 2 nm and that of ∼1.36% for 4 nm, respectively) due to the similar refractive indices of the two polymers (Figure S11). This result clearly indicated that control of polymer thickness was more important than control over composition or shape in order to obtain good sensitivity. Since the thickness was the dominant factor, we estimated the *optimal* thickness as ∼1.75 nm for Au-NP with diameter = 7.6 nm (Figure S12) by assuming that the enhanced electric field beneath the Au-NP surface became the same value as the decayed electric field at the end of the polymer surface.

To investigate coupling effects caused by the closeness of Au-NPs (i.e., with diameter = 7.6 nm) in the dimer, two Au-NPs were separated by varying $D$ values (from $D$ = 24 to 0 nm), where $D$ is the gap distance between surfaces of two Au-NPs. At $D$ = 24 nm, the coupling effect was completely eliminated, and $C_{abs}/2$ became similar to that of the monomer. Note that $C_{abs}/2$ represents the property of the monomer in the dimer. The value of $C_{abs}/2$ and the maximum peak wavelength gradually increased on decreasing $D$ from 24 to 4.2 nm (Figure 5a). The increments of $C_{abs}/2$ and the maximum peak wavelength were continued to $D$ = 1 nm, and then $C_{abs}/2$ reached the maximum but the peak was red-shifted further until $D$ = 0.6 nm (Figure 5b). Enhanced electric fields between Au-NPs were observed due to the coupling of localized surface plasmon resonance (LSPR) of Au-NPs for $D$ = 0.6 nm (Figures 5c and 5d). At $D$ = 0.6 nm, the value of $|E(\omega)|_{max}^2/E_0^2$ of the dimer was 36 times greater than that of the monomer due to the gap-plasmonic effect.[36,37] It is known that $D ≤ 0.4$ nm belongs to the quantum regime,[22] where electron tunneling occurs. To describe the effect of electron tunneling on the plasmon mode, the quantum-corrected model (QCM)[22,23] was implemented to our classical electrodynamics calculation (see Electron Tunneling Effect in the Computational Methods section). At $D$ = 0.2 and 0.4 nm, the absorption peak was split into two, and this was induced by the bonding dipole plasmon (BDP) and high-order hybridized plasmon (HHP) modes (Figure 6a). The latter mode was generated by plasmon hybridization from the interaction of plasmons of different angular momentums of each particle due to a short gap distance; when the dipole-active plasmon mode of one particle interacts with the higher energy level of the other, a new peak with high plasmon energy appears at a low wavelength.[38] Based on this fact, we identified the plasmon modes of the main peaks (i.e., maximum intensity of $C_{abs}/2$), which were the HHP mode
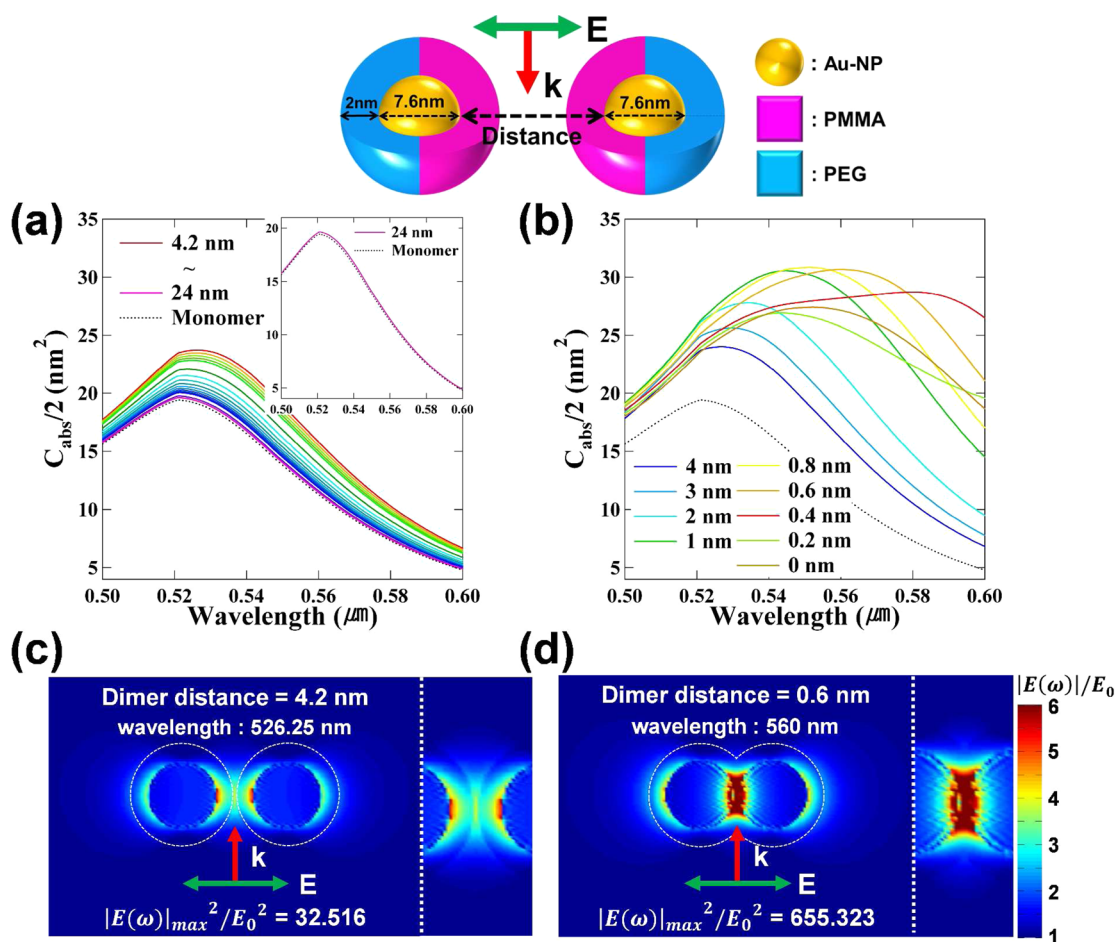
**Figure 5.** Absorption cross sections of the monomer in the dimer ($C_{abs}/2$) with respect to the gap distance ($D$) at (a) 4.2−24 nm and (b) 0−4 nm. (c) and (d) Electric field contour plots at peak wavelengths from the $C_{abs}/2$ spectra for $D$ at (a) 4.2 nm and (b) 0.6 nm, respectively. Directions of the electric field $E$ and the incident light $k$ are indicated with arrows.

for $D$ = 0.2 nm and the BDP mode for $D$ = 0.4 nm. It indicated that, as two particles become closer, the plasmon mode of the main peak changed from BDP to HHP. Interestingly, for the case of $D$ = 0.2 nm, we found that the BDP peak was remarkably decreased because of electron tunneling. It results in the weakening of the plasmon hybridization of bonding and antibonding energy levels in the dipolar mode.

To determine the detection accuracy of the dimer, fwhm's were calculated from $D$ = 0 to 9 nm. Especially for $D \leq 0.4$ nm, we deconvoluted the $C_{abs}/2$ plots to extract the value of intrinsic fwhm's. Upon reducing $D$ to 0.4 nm, the detection accuracy was decreased, as demonstrated by increasing fwhm's of the main peaks at each $D$ (Figure 6b). The greatest improvement in detection accuracy was observed at $D$ = 0.2 nm even under diminishing electron tunneling effects (Inset of Figure 6b). This phenomenon directly resulted from HHP, where the total dephasing time of plasmon resonance was long (Figure 6c). On the other hand, the maximum sensitivity was significantly decreased at $D$ = 0.2 nm, as shown by decreasing $|E(\omega)|_{max}^2/E_0^2$ of the main peak, and the sensitivity was reduced further by the electron tunneling (Figure 6d). Remarkably, $|E(\omega)|_{max}^2/E_0^2$ of the secondary peak (BDP peak) at $D$ = 0.2 nm was larger than that of the main peak (BDP peak) at $D$ = 0.4 nm by ∼33% even under the electron tunneling effect (Figure S13e). Among $D$ = 0, 0.2, and 0.4 nm, $|E(\omega)|_{avg}^2/E_0^2$ of the secondary peak was the largest for $D$ = 0.2 nm, particularly at

the center and edge of the dimer (Figure 6f). These results revealed the ambilateral nature of peaks for sensing application at $D$ = 0.2 nm (i.e., high detection accuracy but low sensitivity at the main (HHP) peak, and low detection accuracy but high sensitivity at the secondary (BDP) peak). We also considered the net change of the sensitivity and the detection accuracy to investigate the optimal gap distance, which showed the high sensing capability through the figure of merit (FOM). In Figure S13a, the FOM value sharply increased from 1 nm and was dropped from 0.4 nm. In particular, from 0.4 to 1.0 nm, the detection accuracy was decreased while the sensitivity was increased. However, from 0.4 to 0.2 nm, the detection accuracy was increased while the sensitivity was decreased (Figure S13b and S13c). Overall, because of greater change of sensitivity compared to detection accuracy, the FOM followed the same trend of sensitivity. Additionally, the secondary peak was also investigated. From 0.4 to 0.2 nm, detection accuracy was decreased while sensitivity was increased (Figure S13b and S13c). Overall, because of greater change of sensitivity compared to detection accuracy, the FOM was increased by following the trend of sensitivity (Figure S13a). From the FOM analysis, we can conclusively remark that the high sensing capability appears indeed at the optimal gap distance between 0.2 and 0.4 nm. At $D$ = 0 nm, the charge transfer plasmon (CTP) mode was dominant[39,40] as inferred by the secondary peak at 1040 nm, since the two Au-NPs acted like a single
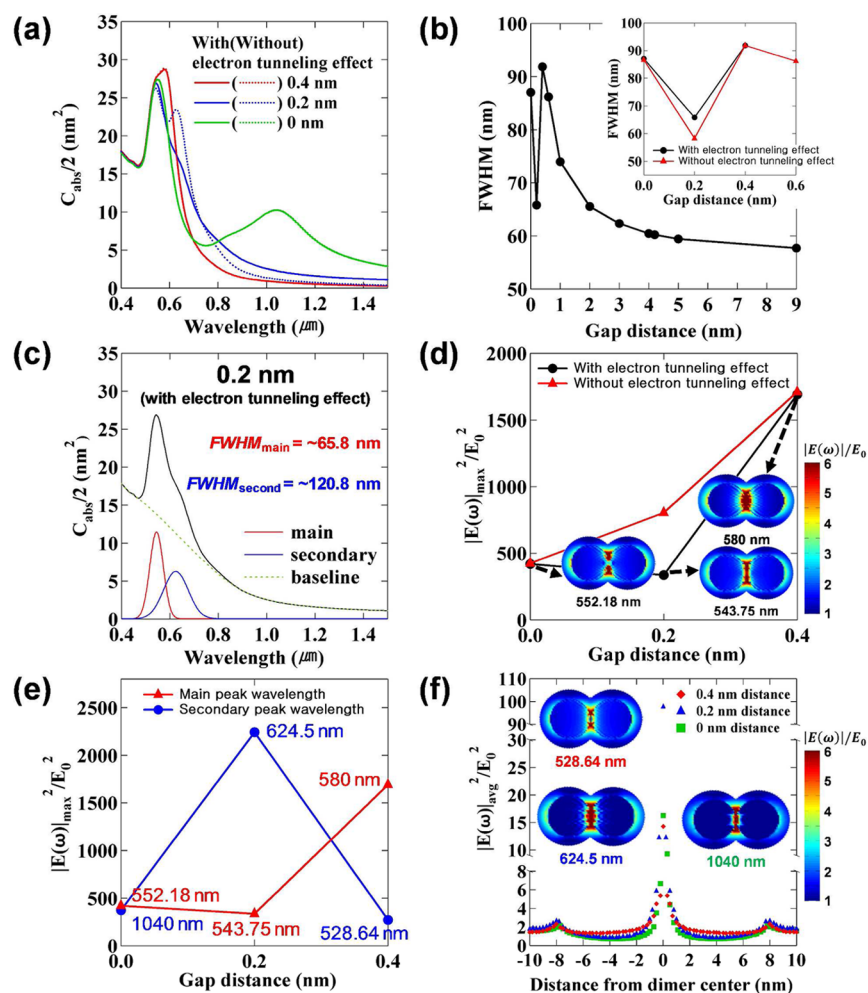
**Figure 6.** (a) Absorption cross section of the monomer in the dimer ($C_{abs}/2$) with respect to the gap distance ($D$) over wavelength. The solid and dashed lines correspond to the presence and absence of the electron tunneling effect, respectively. (b) fwhm of the main peak at each $D$. Inset shows the fwhm results of 0.4, 0.2, and 0 nm with (black line) and without (red line) the electron tunneling effect. (c) Deconvoluted main (red line) and secondary (blue line) plots for $D = 0.2$ nm under the electron tunneling effect using a Gaussian function. The plots were calculated by fixing the secondary peak wavelength, where the second and third derivatives became zero, to find the exact inflection point in the $C_{abs}/2$ spectra.[63,64] (d) $|E(\omega)|_{max}^2/E_0^2$ of 0.4, 0.2, and 0 nm at the main peak wavelength with (black line) and without (red line) the electron tunneling effect. (e) $|E(\omega)|_{max}^2/E_0^2$ of 0.4, 0.2, and 0 nm at the main (red line) and secondary (blue line) peak wavelengths with the electron tunneling effect. (f) $|E(\omega)|_{avg}^2/E_0^2$ at the secondary peak wavelengths of each $D$ (i.e., 0.4, 0.2, and 0 nm) with the electron tunneling effect. The values were calculated by setting the baseline (i.e., principal axis) to be the linearly connected centers of the Au-NPs in the dimer.

particle with a large effective volume, where charge oscillated throughout Au-NPs. Thus, the contact of Au-NPs had a significant impact on the drastic reduction of detection accuracy and sensitivity at the main peak wavelength (Figures 6b and 6d).

## CONCLUSION

We successfully employed DPD, a coarse-grained simulation method, and DDA, a method to estimate the optical properties of plasmonic material, to suggest optimum key factors for sensors based on the Au-NP dimer. First, we have shown the size controllability of Au-NPs in terms of the volume fraction of PMMA and PEG in polymer brushes. The same amount of the amphiphilic polymers induced the formation of the largest Au-NP monomer. From the dimerization study, we have shown that PMMA-like hydrophobic polymers played a linker role in the formation of the dimer, and its amount was a very important factor to ensure good dimerization. The gap distance was controlled by varying PMMA content, and the optimal

dimer model of Au-NP was suggested. The optimal growing condition of dimer was found to be 54.3−64.3 vol % of PMMA. Next, by conducting DDA calculations with inclusion of quantum effects, we could analyze the sensing capabilities of polymer-grafted Au-NP monomer and dimer over a small scale. For the monomer system, we have clearly shown that the two quantum effects (i.e., intrinsic size effect and nonlocal effect) reduced $C_{abs}$, detection accuracy, and sensitivity of bare Au-NP. However, with the polymer shell, even though detection accuracy was reduced only slightly, $C_{abs}$ was considerably increased. Due to the polymer shell, the induced electric field was enhanced and the enhancement was intensified as the polymer thickness increased. For Au-NP with a diameter of 7.6 nm, the optimal thickness was estimated to be 1.75 nm for the best sensitivity. For the dimer system, the distance between Au-NPs played a major role in improving the sensitivity drastically by increasing the electric field intensity through coupling LSPRs. In general, the detection accuracy was low when the gap distance between two monomers ($D$) was above 0.4 nm, but

within the quantum regime, the detection accuracy was maximal at $D$ = 0.2 nm due to the HHP mode even under the electron tunneling effect. The sensitivity, which was elucidated from the electric field intensity, was maximal at $D$ = 0.4 nm, where electron tunneling effects were negligible. Moreover, through the FOM analysis, we demonstrated that the optimal gap distance showed high sensing capability. Overall, therefore, for the best detection accuracy and sensitivity, the suggested gap distance between Au-NPs in the dimer was 0.2−0.4 nm. Even though theoretical analyses have been carried out with a few specific sizes of Au-NPs, we remark that the average size of NPs lied in the range between 2 and 10 nm so that one may expect similar results with similar sizes of Au-NPs. One must note that the DPD and DDA calculations carried out in this study include a few simplifications and approximations originating from the nature of calculation methods. In DPD, coarse-grained feature simplifies the interactions of atoms. In DDA, spatial discretization by dipole points approximates the actual shape of the target system. Thus, it is necessary to validate the applicability of each method to the system of interest by reproducing experimental results as well as theoretical verification through varying coarse-graining degree and dipole spacing. When those parameters are well found, the physical phenomena such as self-assemblies of monomer and dimer and their plasmonic properties could show meaningful results.

## ■ COMPUTATIONAL METHODS

**Dissipative Particle Dynamics (DPD).** DPD, which was developed by Hoogerbrugge and Koelman,[41] uses the concept of superatom depicted as a bead that experiences dissipative, random, and conservative forces. The former two forces are auxiliary functions for the energy sink and source, which work together as a thermostat to maintain the isothermal conditions of the system. The last term represents the soft-repulsive interactions of the beads. The bead physically does not contain molecules but only represents chemical identity of molecules. It can conceptually contain a few to several molecules or fractional parts of material by calculation adequate interpretation of pair interactions of beads. Groot and Warren[42] have realized the interaction based on the repulsion parameter, which originally comes from the difference of solubility parameters of actual molecules. The size of the bead is generally determined by a multiple of the effective volume, where the number of specified water molecules can be fitted. Detailed information on the method can be found in the literature.[42] Hence, we only provide a brief summary of the method. The conservative force undergoes adjustment of a repulsion parameter that is expressed as follows

$$a_{ii} = \frac{(\kappa^{-1}N_m - 1)}{2\alpha\rho}k_BT \tag{1}$$

$$a_{ij} = a_{ii} + 3.27\chi_{ij} \tag{2}$$

$$\chi_{ij} = \frac{V_{bead}}{k_BT}(\delta_i - \delta_j)^2 \tag{3}$$

where $a_{ii}$ and $a_{ij}$ are the repulsion parameters for the same and different types of beads, respectively, $\kappa$ is the isothermal compressibility of water, $N_m$ is the number of basis molecules (i.e., water in this study) included in a bead, $\rho$ is the bead number density, $\alpha$ is a fitting constant, $k_B$ is the Boltzmann's

constant, $T$ is the temperature, $\chi_{ij}$ is the Flory−Huggins parameter, $V_{bead}$ is the bead volume, and $\delta_i$ and $\delta_j$ are the solubility parameters for different types of beads.[28] The values fitted to our model systems are $\kappa^{-1}$ = 16, $N_m$ = 12, $\rho$ = 3, and $\alpha$ = 0.1 with $V_{bead}$ = 0.36 nm$^3$ that is equivalent to the volume of 12 water molecules. First, the solubility parameter was obtained from the cohesive energy density (CED) from $\delta = \sqrt{CED}$. We have performed all-atom molecular dynamics (MD) simulation to obtain CED for each component (i.e., water, constitutional units of PEG and PMMA) at 298 K. For PEG and PMMA, the solubility parameters were determined by checking the number of constitutional units in a bead (Figure S1). Each MD simulation was run for at least 1 ns with a time step of 1 fs. Sequential runs of NPT (i.e., isothermal−isobaric) and NVT (i.e., isothermal) MD simulations were performed with the Berendsen thermostat and barostat.[43,44] After the equilibration, additional NVT MD was run to obtain the final CEDs. For the simulation, we used the COMPASS force field.[45] Table S1 shows the calculated repulsion parameters. Note that the solubility parameter of Au (i.e., 4.865 (J cm$^{-3}$)$^{0.5}$) was extracted from the work of Chen et al.[28] where the Au−water repulsion parameter was estimated to be 825.31. The DPD interaction radius ($R_c$) was set to 1.026 nm based on the bead density (i.e., $\rho$ = 3), where three beads were contained in a box volume of 1.08 nm. In DPD, $R_c$ represents the cutoff range of the interaction distance between beads. Since the constituent atoms, molecules, and constitutional units in the beads have different volumes, we controlled the numbers of each component to be included into a roughly same $V_{bead}$. Figure 1a shows the information on the beads of the components. Note that the numbers of constitutional units in the polymers are not required to be integers because the same types of constitutional units are sequentially connected in the polymers.[46] For chain lengths of polymers in DPD, PMMA and PEG were set to be 110 and 22 for the study of monomer Au-NP and 118 and 22 for that of dimer Au-NP, respectively, which are estimated from experimental results.[20,47] The bond between polymer beads was assumed to be harmonic with a dimensionless spring constant varying between 4 (2.25 kcal mol/nm$^2$) and 6 (i.e., 3.37 kcal mol/nm$^2$), which was used to preserve the chain form of polymers. To include the grafting effect, one Au bead was attached to the ends of the polymer bead models. For the self-assembly simulation of the monomer and dimer of Au-NP, the simulation box sizes were set to 20 × 20 × 20 $R_c^3$ and 26 × 26 × 26 $R_c^3$, which contained 25 725 and 51 110 beads, respectively. The periodic boundary condition was applied to the simulation box. We ran DPD simulations about 200 ns on average except 400 ns for the dimer simulation with a dimensionless time step of 0.01 (i.e., 95.795 fs) in units of $R_c\sqrt{m_{bead}/k_BT}$, where $m_{bead}$ was the mass of bead (i.e., 216 amu). All simulations were conducted at room temperature.

**Discrete Dipole Approximation (DDA).** DDA, which allows us to investigate optical properties of extinction, absorption, and scattering, divides an arbitrarily shaped target system into a finite array of dipole points, which are formulated to have dipole moments by the local electric field. After DeVoe introduced DDA,[48,49] Purcell and Pennypacker have advanced this method by incorporating the retardation phenomenon,[50] which occurred if the size of the particle was larger than 10% of the wavelength.[51] We briefly explain the DDA method in the following derivation.[29,52] First, a target structure is divided into

an array of $N$ dipole points, and then the dipole moment $P_i$ is calculated by the following equation

$$P_i = \alpha_i \cdot E_{loc}(r_i) \tag{4}$$

where $\alpha_i$ is the polarizability tensor, which is based on Clausius−Mossotti polarizability,[29,50] and $E_{loc}(r_i)$ is the external electric field with $i = 1, 2, 3, ..., N$. The local electric field (i.e., $E_{loc}(r_i)$) is composed by the sum of incident field and dipole field as follows

$$P_i = \alpha_i \cdot \left( E_{inc,i} - \sum_{\substack{j=1 \\ i \neq j}}^{N} A_{ij} \cdot P_j \right) \tag{5}$$

where $E_{inc,i}$ is the incident electric field at position $r_i$ and $A_{ij}$ is an arbitrary $3 \times 3$ matrix. By solving the dipole moment $P_i$ in eq 5, the optical properties of absorption cross sections (i.e., $C_{abs}$) can be calculated through the following equation

$$C_{abs} = \frac{4\pi k}{|E_{inc}|^2} \sum_{j=1}^{N} \left\{ Im[P_j \cdot (\alpha_j^{-1})^* \cdot P_j^*] - \frac{2}{3} k^3 P_j \cdot P_j^* \right\} \tag{6}$$

where superscript * represents the conjugate value of each property. To execute the theory, we used the DDSCAT program (v 7.3.0) originally developed by Drain and Flatau.[29] There is a criterion $|m|kd < 1$, in which optical properties calculated by DDSCAT become trustworthy, where $|m|$ is the complex refractive index, $k$ is the reciprocal value of incident wavelength, and $d$ is the dipole spacing between adjacent dipoles. The dielectric functions of PMMA and PEG were taken from literature.[53,54] On the other hand, the dielectric function of Au was estimated by considering the radius ($R$) of Au-NP and the gap distance ($l$) of the Au-NP dimer system due to quantum effects. The dielectric function of gold depending on the $R$ of Au-NP due to intrinsic size effect and nonlocal effect is as follows

$$\varepsilon_{free\text{-}electrons}(k, \omega, R) = 1 - \frac{\omega_p^2}{\omega(\omega + i\gamma_{free}(R)) - \beta^2 k^2} \tag{7}$$

Moreover, the dielectric function to describe the electron tunneling effect depending on the $l$ of Au-NP dimer system is as follows

$$\varepsilon_g(\omega, l) = \varepsilon_0(\omega) + (\varepsilon_m^d(\omega) - \varepsilon_0(\omega))e^{-l/l_d}$$
$$- \frac{\omega_p^2}{\omega(\omega + i\gamma_g(l))} \tag{8}$$

We applied three quantum effects (i.e., intrinsic size effect, nonlocal effect, and electron tunneling effect) in the DDA calculation. More detailed explanations of each quantum effect are introduced in each quantum effect section below.

**Intrinsic Size Effect.** The radius of Au-NP in our target model was 3.8 nm, which was in the quantum effect region. Generally, the bulk dielectric function of noble metals can be described by the following equation:[55,56]

$$\varepsilon_{bulk}(\omega) = \varepsilon_{bound\text{-}electrons}(\omega) + \varepsilon_{free\text{-}electrons}(\omega) \tag{9}$$

The dielectric function of the bound-electrons term ($\varepsilon_{bound\text{-}electrons}(\omega)$) includes the interband transitions from the d-band to the conduction sp-band. If the radius of the particle is

over 1 nm, the term does not depend on the size of the particle.[55] Thus, we did not consider the size dependence of bound-electrons term in this paper. The other term, which comes from free-electrons ($\varepsilon_{free\text{-}electrons}(\omega)$), is expressed with the Drude−Sommerfeld model as follows

$$\varepsilon_{free\text{-}electrons}(\omega) = 1 - \frac{\omega_P^2}{\omega^2 + i\gamma_{free}\omega} \tag{10}$$

where $\omega_p$ is the bulk plasma frequency and $\gamma_{free}$ is the damping constant. The value of $\omega_p$ for Au is $1.3 \times 10^{16}$ Hz.[57] The intrinsic size effect can be estimated by changing the damping constant depending on the size of the particle

$$\gamma_{free}(R) = \gamma_{bulk} + C\frac{v_F}{R} \tag{11}$$

where $v_F$ is the electron velocity at the Fermi surface, $R$ is the radius of the particle, and $C$ is the scattering constant, which is included in the scattering processes.[55] The value of $C$ depends on the geometry of the particle. In this paper, we used the spherical particle, where $C$ was 0.75.[58] $v_F$ of Au was $1.41 \times 10^{15}$ nm s$^{-1}$,[57] and the bulk damping constant ($\gamma_{bulk}$) was $1.1 \times 10^{14}$ Hz.[59]

**Nonlocal Effect.** The nonlocal effect can be expressed by applying the hydrodynamic Drude model[60−62] to the Drude−Sommerfeld model

$$\varepsilon_{free\text{-}electrons}(k, \omega) = 1 - \frac{\omega_p^2}{\omega(\omega + i\gamma_{free}) - \beta^2 k^2} \tag{12}$$

where $\beta^2$ is expressed by $\frac{Av_F^2}{D}$, where $D$ is the dimension of the target structure, $A$ is 1 for low frequencies, and $\frac{3D}{D+2}$ for high frequencies. In this paper, we used a spherical particle, which was a three-dimensional structure, with size in the range of the incident light wavelength (0.4−0.8 $\mu$m). Therefore, the values of $D$ and $A$ were taken to be 3 and 1.8, respectively. $k$ is the wave-vector component, which is expressed by $2\pi/b$, where $b$ is the particle size. In short, we used the size-corrected Drude−Sommerfeld model that includes the two quantum effects, namely intrinsic size effect and nonlocal effect as follows:

$$\varepsilon_{free\text{-}electrons}(k, \omega, R) = 1 - \frac{\omega_P^2}{\omega(\omega + i\gamma_{free}(R)) - \beta^2 k^2} \tag{13}$$

**Electron Tunneling Effect.** In the dimer system, when the gap distance is below 0.4 nm, they belong to the quantum regime, where electron tunneling occurs between Au-NPs. To describe this effect in the classical electrodynamics calculation, we used the quantum-corrected model (QCM).[22,23] The QCM is to make the artificial medium (i.e., effective medium for electron tunneling effect) between adjacent two Au-NPs in the dimer. By using the dielectric function of this medium, which depends on the frequency ($\omega$) and gap distance ($l$), the electron tunneling effect can be described. The permittivity $\varepsilon_g(\omega, l)$ can be expressed as follows[22]

$$\varepsilon_g(\omega, l) = \varepsilon_0(\omega) + (\varepsilon_m^d(\omega) - \varepsilon_0(\omega))e^{-l/l_d}$$
$$- \frac{\omega_P^2}{\omega(\omega + i\gamma_g(l))} \tag{14}$$

where $\gamma_g(l)$ is the gap distance-dependent loss parameter.[22] It can be expressed as follows

$$\gamma_g(l) = \gamma_p e^{l/l_c} \tag{15}$$

where $l_c$ is the characteristic length, $l_d$ is the decay length, and $\varepsilon_0(\omega)$ and $\varepsilon_m^d(\omega)$ are the dielectric functions of dielectric medium and interband transitions, respectively. For Au metal, the value of $l_c$ was 0.4 Å.[22] For $\gamma_p$, we used $\gamma_{free}(R)$ from the intrinsic size effect section. $l_d$ was 0.79 Å.[22] In this paper, we applied the QCM to dimer systems, where the gap distances were 0.4, 0.2, and 0 nm. Also, the dielectric medium was PMMA because the tunneling region was occupied with PMMA polymer. All systems for the DDA calculation were constructed with 0.2 nm of dipole spacing ($d$) and were conducted in water environment. The ranges of wavelengths were 0.4–0.8 $\mu$m for monomer systems and 0.5–0.6 $\mu$m for dimer systems except for dimer systems below 0.4 nm, in which the range of wavelength was extended to 1.5 $\mu$m.

## ■ ASSOCIATED CONTENT

**⑤ Supporting Information**

The Supporting Information is available free of charge on the ACS Publications website at DOI: 10.1021/acs.jpcc.6b01055.

Supporting figures and tables (PDF)

## ■ AUTHOR INFORMATION

**Corresponding Authors**

*E-mail: bskim19@unist.ac.kr. Tel.: +82-52-217-2923.
*E-mail: msyeom@kisti.re.kr. Tel.: +82-42-869-0614.
*E-mail: skkwak@unist.ac.kr. Tel.: +82-52-217-2541.

**Author Contributions**

$^\perp$These authors contributed equally.

**Notes**

The authors declare no competing financial interest.

## ■ ACKNOWLEDGMENTS

## ■ REFERENCES

(1) Oh, E.; Susumu, K.; Goswami, R.; Mattoussi, H. One-Phase Synthesis of Water-Soluble Gold Nanoparticles with Control over Size and Surface Functionalities. *Langmuir* **2010**, *26*, 7604–7613.

(2) Jana, N. R.; Gearheart, L.; Murphy, C. J. Seed-Mediated Growth Approach for Shape-Controlled Synthesis of Spheroidal and Rodlike Gold Nanoparticles Using a Surfactant Template. *Adv. Mater.* **2001**, *13*, 1389–1393.

(3) Mayer, K. M.; Hafner, J. H. Localized Surface Plasmon Resonance Sensors. *Chem. Rev.* **2011**, *111*, 3828–3857.

(4) Rosi, N. L.; Mirkin, C. A. Nanostructures in Biodiagnostics. *Chem. Rev.* **2005**, *105*, 1547–1562.

(5) Hainfeld, J. F.; Furuya, F. R. A 1.4-nm Gold Cluster Covalently Attached to Antibodies Improves Immunolabeling. *J. Histochem. Cytochem.* **1992**, *40*, 177–184.

(6) Anker, J. N.; Hall, W. P.; Lyandres, O.; Shah, N. C.; Zhao, J.; Van Duyne, R. P. Biosensing with Plasmonic Nanosensors. *Nat. Mater.* **2008**, *7*, 442–453.

(7) Lasne, D.; Blab, G. A.; Berciaud, S.; Heine, M.; Groc, L.; Choquet, D.; Cognet, L.; Lounis, B. Single Nanoparticle Photothermal

(8) Jain, P. K.; Lee, K. S.; El-sayed, I. H.; El-sayed, M. A. Calculated Absorption and Scattering Properties of Gold Nanoparticles of Different Size, Shape, and Composition: Applications in Biological Imaging and Biomedicine. *J. Phys. Chem. B* **2006**, *110*, 7238–7248.

(9) Manimaran, M.; Jana, N. R. Detection of Protein Molecules by Surface-Enhanced Raman Spectroscopy-Based Immunoassay using 2–5 nm Gold Nanoparticle Lables. *J. Raman Spectrosc.* **2007**, *38*, 1326–1331.

(10) Kreibig, U.; Vollmer, M. *Optical Properties of Metal Clusters*; Springer-Verlag: Berlin, 1995.

(11) Hayat, M. A. *Immunogold-Silver Staining: Principles, Methods, and Applications*; Academic Press: New York, 1995.

(12) Ma, Z.; Sui, S. F. Naked-Eye Sensitive Detection of Immunoglubulin G by Enlargement of Au Nanoparticles in Vitro. *Angew. Chem., Int. Ed.* **2002**, *41*, 2176–2179.

(13) Su, K. H.; Wei, Q. H.; Zhang, X.; Mock, J. J.; Smith, D. R.; Schultz, S. Interparticle Coupling Effects on Plasmon Resonances of Nanogold Particles. *Nano Lett.* **2003**, *3*, 1087–1090.

(14) Nie, Z.; Fava, D.; Kumacheva, E.; Zou, S.; Walker, G. C.; Rubinstein, M. Self-Assembly of Metal–Polymer Analogues of Amphiphilic Triblock Copolymers. *Nat. Mater.* **2007**, *6*, 609–614.

(15) Posocco, P.; Posel, Z.; Fermeglia, M.; Lisal, M.; Pricl, S. A Molecular Simulation Approach to the Prediction of the Morphology of Self-Assembled Nanoparticles in Diblock Copolymers. *J. Mater. Chem.* **2010**, *20*, 10511–10520.

(16) Sakai, T.; Alexandridis, P. Single-Step Synthesis and Stabilization of Metal Nanoparticles in Aqueous Pluronic Block Copolymer Solutions at Ambient Temperature. *Langmuir* **2004**, *20*, 8426–8430.

(17) Hussain, I.; Graham, S.; Wang, Z.; Tan, B.; Sherrington, D. C.; Rannard, S. P.; Cooper, A. I.; Brust, M. Size-Controlled Synthesis of Near-Monodisperse Gold Nanoparticles in the 1–4 nm Range using Polymeric Stabilizers. *J. Am. Chem. Soc.* **2005**, *127*, 16398–16399.

(18) Cai, C.; Wang, L.; Lin, J.; Zhang, X. Morphology Transformation of Hybrid Micelles Self-Assembled from Rod-Coil Block Copolymer and Nanoparticles. *Langmuir* **2012**, *28*, 4515–4524.

(19) Zubarev, E. R.; Xu, J.; Sayyad, A.; Gibson, J. D. Amphiphilicity-Driven Organization of Nanoparticles into Discrete Assemblies. *J. Am. Chem. Soc.* **2006**, *128*, 15098–15099.

(20) Cheng, L.; Liu, A.; Peng, S.; Duan, H. Responsive Plasmonic Assemblies of Amphiphilic Nanocrystals at Oil–Water Interfaces. *ACS Nano* **2010**, *4*, 6098–6104.

(21) Du, C. L.; Yang, M. X.; You, Y. M.; Chen, T.; Chen, H. Y.; Shen, Z. X. Polymer-Encapsulated Silver Nanoparticle Monomer and Dimer for Surface-Enhanced Raman Scattering. *Chem. Phys. Lett.* **2009**, *473*, 317–320.

(22) Esteban, R.; Zugarramurdi, A.; Zhang, P.; Nordlander, P.; Garcia-Vidal, F. J.; Borisov, A. G.; Aizpurua, J. A Classical Treatment of Optical Tunneling in Plasmonic Gaps: Extending the Quantum Corrected Model to Practical Situations. *Faraday Discuss.* **2015**, *178*, 151–183.

(23) Esteban, R.; Borisov, A. G.; Nordlander, P.; Aizpurua, J. Bridging Quantum and Classical Plasmonics with a Quantum-Corrected Model. *Nat. Commun.* **2012**, *3*, 825.

(24) Yamamoto, S.; Maruyama, Y.; Hyodo, S. Dissipative Particle Dynamics Study of Spontaneous Vesicle Formation of Amphiphilic Molecules. *J. Chem. Phys.* **2002**, *116*, 5842–5849.

(25) Zhao, Y.; You, L. Y.; Lu, Z. Y.; Sun, C. C. Dissipative Particle Dynamics Study on the Multicompartment Micelles Self-Assembled from the Mixture of Diblock Copolymer Poly(ethyl ethylene)-Block-Poly(ethylene oxide) and Homopolymer Poly(propylene oxide) in Aqueous Solution. *Polymer* **2009**, *50*, 5333–5340.

(26) Liu, D.; Zhong, C. Macromol. Cooperative Self-Assembly of Nanoparticle Mixtures in Lamellar Diblock Copolymers: A Dissipative Particle Dynamics Study. *Macromol. Rapid Commun.* **2006**, *27*, 458–462.

(27) Juan, S. C. C.; Hua, C. Y.; Chen, C. L.; Sun, X. Q.; Xi, H. T. Dissipative Particle Dynamics Simulation of a Gold Nanoparticle System. *Mol. Simul.* **2005**, *31*, 277–282.

(28) Chen, S.; Hu, G. H.; Guo, C.; Liu, H. Z. Experimental Study and Dissipative Particle Dynamics Simulation of the Formation and Stabilization of Gold Nanoparticles in PEO–PPO–PEO Block Copolymer Micelles. *Chem. Eng. Sci.* **2007**, *62*, 5251–5256.

(29) Draine, B. T.; Flatau, P. J. Discrete-Dipole Approximation for Scattering Calculations. *J. Opt. Soc. Am. A* **1994**, *11*, 1491–1499.

(30) Frisman, I.; Orbach, R.; Seliktar, D.; Bianco-Peled, H. Structural Investigation of PEG-Fibrinogen Conjugates. *J. Mater. Sci.: Mater. Med.* **2010**, *21*, 73–80.

(31) De Gennes, P. G. *Scaling Concepts in Polymer Physics*; Cornell University Press: Ithaca, NY, 1979.

(32) Paine, A. J. Dispersion Polymerization of Styrene in Polar Solvents. 7. A Simple Mechanistic Model to Predict Particle Size. *Macromolecules* **1990**, *23*, 3109–3117.

(33) Ghosh, S. K.; Pal, T. Interparticle Coupling Effect on the Surface Plasmon Resonance of Gold Nanoparticles: From Theory to Applications. *Chem. Rev.* **2007**, *107*, 4797–4862.

(34) Zhao, Y.; Hu, X.; Chen, G.; Zhang, X.; Tan, Z.; Chen, J.; Ruoff, R. S.; Zhu, Y.; Lu, Y. Infrared Biosensors Based on Graphene Plasmonics: Modeling. *Phys. Chem. Chem. Phys.* **2013**, *15*, 17118–17125.

(35) Link, S.; El-Sayed, M. A. Size and Temperature Dependence of the Plasmon Absorption of Colloidal Gold Nanoparticles. *J. Phys. Chem. B* **1999**, *103*, 4212–4217.

(36) Solis, D. M.; Taboada, J. M.; Obelleiro, F.; Liz-Marzan, L. M.; Garcia de Abajo, F. J. Toward Ultimate Nanoplasmonics Modeling. *ACS Nano* **2014**, *8*, 7559–7570.

(37) Alexander, K. D.; Skinner, K.; Zhang, S.; Wei, H.; Lopez, R. Tunable SERS in Gold Nanorod Dimers through Strain Control on an Elastomeric Substrate. *Nano Lett.* **2010**, *10*, 4488–4493.

(38) Nordlander, P.; Oubre, C.; Prodan, E.; Li, K.; Stockman, M. I. Plasmon Hybridization in Nanoparticle. *Nano Lett.* **2004**, *4*, 899–903.

(39) Wang, Y.; Li, Z.; Zhao, K.; Sobhani, A.; Zhu, X.; Fang, Z.; Halas, N. J. Substrate-Mediated Charge Transfer Plasmons in Simple and Complex Nanoparticle Clusters. *Nanoscale* **2013**, *5*, 9897–9901.

(40) Wen, F.; Zhang, Y.; Gottheim, S.; King, N. S.; Zhang, Y.; Nordlander, P.; Halas, N. J. Charge Transfer Plasmons: Optical Frequency Conductances and Tunable Infrared Resonances. *ACS Nano* **2015**, *9*, 6428–6435.

(41) Hoogerbrugge, P. J.; Koelman, J. M. V. A. Simulating Microscopic Hydrodynamic Phenomena with Dissipative Particle Dynamics. *Europhys. Lett.* **1992**, *19*, 155–160.

(42) Groot, R. D.; Warren, P. B. Dissipative Particle Dynamics: Bridging the Gap between Atomistic and Mesoscopic Simulation. *J. Chem. Phys.* **1997**, *107*, 4423–4435.

(43) Allen, M. P.; Tildesley, D. J. *Computer Simulation of Liquids*; Clarendon Press: Oxford, 1987.

(44) Berendsen, H. J. C.; Postma, J. P. M.; van Gunsteren, W. F.; DiNola, A.; Haak, J. R. Molecular Dynamics with Coupling to an External Bath. *J. Chem. Phys.* **1984**, *81*, 3684–3690.

(45) Sun, H. COMPASS: An ab Initio Force-Field Optimized for Condensed-Phase Applications—Overview with Details on Alkane and Benzene Compounds. *J. Phys. Chem. B* **1998**, *102*, 7338–7364.

(46) Groot, R. D.; Rabone, K. L. Mesoscopic Simulation of Cell Membrane Damage, Morphology Change, and Rupture by Nonionic Surfactants. *Biophys. J.* **2001**, *81*, 725–736.

(47) Cheng, L.; Song, J.; Yin, J.; Duan, H. Self-Assembled Plasmonic Dimers of Amphiphilic Gold Nanocrystals. *J. Phys. Chem. Lett.* **2011**, *2*, 2258–2262.

(48) Devoe, H. Optical Properties of Molecular Aggregates. I. Classical Model of Electronic Absorption and Refraction. *J. Chem. Phys.* **1964**, *41*, 393–400.

(49) Devoe, H. Optical Properties of Molecular Aggregates. II. Classical Theory of the Refraction, Absorption, and Optical Activity of Solutions and Crystals. *J. Chem. Phys.* **1965**, *43*, 3199–3208.

(50) Purcell, E. M.; Pennypacker, C. R. Scattering and Absorption of Light by Nonspherical Dielectric Grains. *Astrophys. J.* **1973**, *186*, 705–714.

(51) Turner, M. D.; Hossain, M. M.; Gu, M. The Effects of Retardation on Plasmon Hybridization within Metallic Nanostructures. *New J. Phys.* **2010**, *12*, 083062.

(52) Draine, B. T. The Discrete-Dipole Approximation and Its Application to Interstellar Graphite Grains. *Astrophys. J.* **1988**, *333*, 848–872.

(53) Kasarova, S. N.; Sultanova, N. G.; Ivanov, C. D.; Nikolov, I. D. Analysis of the Dispersion of Optical Plastic Materials. *Opt. Mater.* **2007**, *29*, 1481–1490.

(54) Wang, H.; Reinhard, B. M. Monitoring Simultaneous Distance and Orientation Changes in Discrete Dimers of DNA Linked Gold Nanoparticles. *J. Phys. Chem. C* **2009**, *113*, 11215–11222.

(55) Scaffardi, L. B.; Tocho, J. O. Size Dependence of Refractive Index of Gold Nanoparticles. *Nanotechnology* **2006**, *17*, 1309–1315.

(56) Scaffardi, L. B.; Pellegri, N.; de Sanctis, O.; Tocho, J. O. Sizing Gold Nanoparticles by Optical Extinction Spectroscopy. *Nanotechnology* **2005**, *16*, 158–163.

(57) Granqvist, C. G.; Hunderi, O. Optical Properties of Ultrafine Gold Particles. *Phys. Rev. B* **1977**, *16*, 3513–3534.

(58) Coronado, E. A.; Schatz, G. C. Surface Plasmon Broadening for Arbitrary Shape Nanoparticles: A Geometrical Probability Approach. *J. Chem. Phys.* **2003**, *119*, 3926–3934.

(59) Johnson, P. B.; Christy, R. W. Optical Constants of the Noble Metals. *Phys. Rev. B* **1972**, *6*, 4370–4379.

(60) McMahon, J. M.; Gray, S. K.; Schatz, G. C. Calculating Nonlocal Optical Properties of Structures with Arbitrary Shape. *Phys. Rev. B: Condens. Matter Mater. Phys.* **2010**, *82*, 035423.

(61) McMahon, J. M.; Gray, S. K.; Schatz, G. C. Nonlocal Optical Response of Metal Nanostructures with Arbitrary Shape. *Phys. Rev. Lett.* **2009**, *103*, 097403.

(62) Boardman, A. D. *Electromagnetic Surface Modes*; Wiley: New York, 1982.

(63) Maddams, W. F. The Scope and Limitations of Curve Fitting. *Appl. Spectrosc.* **1980**, *34*, 245–267.

(64) de Aragão, B. J. G.; Messaddeq, Y. Peak Separation by Derivative Spectroscopy Applied to FTIR Analysis of Hydrolized Silica. *J. Braz. Chem. Soc.* **2008**, *19*, 1582–1594.

(65) Lifshitz, I. M.; Slyozov, V. V. The Kinetics of Precipitation from Supersaturated Solid Solutions. *J. Phys. Chem. Solids* **1961**, *19*, 35–50.